









The Design, Realization, and Validation of the Scheme for Quantum Degenerate Research in Microgravity

Lin Li , Wei Xiong , Bin Wang , Tang Li , Yu Xie , Angang Liang , Mingshan Huang , Xiaolong Yuan, Yuanyuan Liu, Jingwei Ji, Min Gao, Minjie Huang, Cuiyun Zhou, Tiejing Song, Xingping Xu, Zhaogang Liang, Su Fang, Dijun Chen, Xia Hou, Xiaoji Zhou, Xuzong Chen , Weibiao Chen, and Liang Liu

Abstract—In microgravity, atoms can be prepared to a lower temperature and manipulated with a longer time. The Cold Atom Physics Research Rack (CAPR) in Chinese Space Station, which aims to prepare quantum degenerate gas for deep cooling and quantum simulation in microgravity, has been designed, realized, and validated. We built an integrated CAPR, consisting of a physical system, an all-fiber 780 nm laser system and a low phase noise 1064 nm fiber laser system, and an electrical driving and controlling system. With the CAPR, a ^{87}Rb quantum degenerate gas with 1.2×10^5 atoms and a temperature below 30 nK was achieved on ground. In this article, we also show the robustness of the rack, based on the experimental results before and after the simulation of the vibration and impact during the launch.

Index Terms—Bose-Einstein condensate in microgravity, ultra-cold atom, all-fiber laser system, the cold atom physics research rack in Chinese space station.

I. INTRODUCTION

THE artificial lowest temperature is the eternal pursuit of scientists. Since the beginning of the 20th century, many exciting novel physical phenomena have emerged with low temperature matter, such as superconductivity [1], super fluidity [2], [3], Bose-Einstein condensate (BEC) [4], and degenerate Fermi gas [5]. The lower temperature cold atoms result in longer interrogation time, which is the key of application for atom-based precision measurements [6], [7], [8]. With the development of advanced cooling and trapping technologies such as optical molasses [9], [10], velocity-selectivity coherent population trapping [11], evaporative cooling [4], [5], and Raman cooling [12], the temperature of atoms decreases from room-temperature to micro-kelvin and then to nano-kelvin. By adiabatically decompressing the trap [13] and spin gradient cooling [14], the temperature of the atoms reached hundreds of pico-kelvins. Comparing with the former experiments on ground, lower temperature atomic gas can be realized in microgravity [15], [16], [17].

In recent decades, state-of-the-art experimental platforms have been built to explore the lower temperature of cold atoms and their application in microgravity, such as the drop towers [18], [19], [20], Einstein elevators [21], [22], parabolic flights [23], [24], [25], [26], sounding rockets [27], [28], the TianGong-2 space laboratory [29] and the International Space Station (ISS) [16], [17], [30], [31]. The first BEC in microgravity [18] and its application in Mach-Zehnder interferometers [19] were conducted in the Bremen drop tower using an atom chip. An atomic temperature of about 38 pK was reported, using collective-mode enhanced matter-wave optics and delta-kick collimation [15]. The realization of BEC by optical dipole trap [32], [33] has been demonstrated in an Einstein Elevator [22]. In parabolic flights, the first cold-atom interferometry in microgravity with temperature about 300 nK was realized [25], and the simultaneous ^{87}Rb - ^{39}K interferometer was demonstrated [26]. The first BEC in space was realized in a sounding rocket, and its temperature reached 100 nK during 6 minutes of microgravity [27]. A cold

Manuscript received 25 January 2023; revised 6 April 2023; accepted 7 April 2023. Date of publication 10 April 2023; date of current version 28 April 2023. This work was supported in part by China Manned Space Engineering Office and in part by the Chinese Academy of Sciences. (Corresponding authors: Wei Xiong; Bin Wang; Tang Li.)

Lin Li, Yu Xie, Angang Liang, and Mingshan Huang are with the key Laboratory of Quantum Optics and Center of Cold Atom Physics, Shanghai Institute of Optics and Fine Mechanics, Chinese Academy of Sciences, Shanghai 201800, China, also with the Space Laser Engineering Department, Shanghai Institute of Optics and Fine Mechanics, Chinese Academy of Sciences, Shanghai 201800, China, and also with the Center of Materials Science and Optoelectronics Engineering, University of Chinese Academy of Sciences, Beijing 00049, China (e-mail: linli@siom.ac.cn; xieyu@siom.ac.cn; aaliang@siom.ac.cn; mshuang@siom.ac.cn).

Wei Xiong, Xiaolong Yuan, Xiaoji Zhou, and Xuzong Chen are with the School of Electronics, Peking University, Beijing 100871, China (e-mail: xiongwei@pku.edu.cn; xiaolongyuan@pku.edu.cn; xjzhou@pku.edu.cn; xuzongchen@pku.edu.cn).

Bin Wang, Tang Li, Yuanyuan Liu, Jingwei Ji, Min Gao, Minjie Huang, Cuiyun Zhou, Tiejing Song, Xingping Xu, Zhaogang Liang, Su Fang, Dijun Chen, and Xia Hou are with the Space Laser Engineering Department, Shanghai Institute of Optics and Fine Mechanics, Chinese Academy of Sciences, Shanghai 201800, China (e-mail: wangbin@siom.ac.cn; litang@siom.ac.cn; liuyuanyuan@siom.ac.cn; jijingwei@siom.ac.cn; gaomin@siom.ac.cn; hmj0606@163.com; zhoucuiyun536@163.com; songtiejing@siom.ac.cn; irenexu@mail.siom.ac.cn; lzg@siom.ac.cn; fangsu@siom.ac.cn; djchen@siom.ac.cn; hou_xia@siom.ac.cn).

Weibiao Chen is with the Shanghai Institute of Optics and Fine Mechanics, Chinese Academy of Sciences, Shanghai 201800, China (e-mail: wbchen@mail.shcnc.ac.cn).

Liang Liu is with the key Laboratory of Quantum Optics and Center of Cold Atom Physics, Shanghai Institute of Optics and Fine Mechanics, Chinese Academy of Sciences, Shanghai 201800, China, also with the Space Laser Engineering Department, Shanghai Institute of Optics and Fine Mechanics, Chinese Academy of Sciences, Shanghai 201800, China (e-mail: liang.liu@siom.ac.cn).

Digital Object Identifier 10.1109/JPHOT.2023.3266108

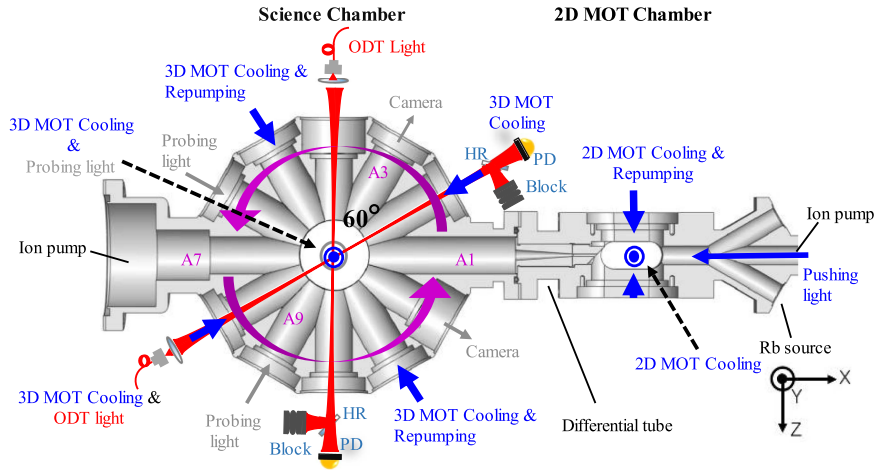


Fig. 1. The scheme of the physical system for CAPR. The physical system consists of two chambers, the 2-D-MOT chamber and the science chamber, which are connected by a differential tube. The science chamber features a dodecagon design and the 2-D MOT chamber is a cuboid. Five optical ports are reserved on the 2-D MOT chamber to feed the pushing light and the 2-D MOT light, including the cooling light and the repumping light. The pushing light travels along the x-direction and pushes atoms into the science chamber. The 2-D MOT optical modules feed the lights into 2-D MOT chamber along the y- and z-direction. The optical modules attached to the science chamber provide the 3-D MOT cooling light, the repumping light, the ODT light, the probing light and so on. Twelve optical ports are reserved in the science chamber in the x-z plane. The optical port connected to the 2-D chamber is named A1, and all twelve ports are named in counterclockwise order from A1 to A12. The angle between two adjacent ports is 30 degrees. Four 3-D MOT cooling beams travel through ports A2, A5, A8 and A11, and the rest two along the y-direction. Ports A4 and A8 are used for ODT beams, and the optical absorbers and photodiodes are located at ports A10 and A2. There are three absorption imaging systems, including the probing lights and the cameras, two of which are aligned in the A3-A9 and A6-A12 directions and the other in the y-direction.

atom clock was demonstrated in Tiangong-2 [29]. The Cold Atom Lab (CAL) was built and launched into the ISS in 2018. A ^{87}Rb BEC with a kinetic energy temperature of 52pK was realized [17], and ultra-cold bubbles were created by inflating smaller condensates [34], [35].

In the Chinese Space Station (CSS), the CAPR, which uses an all-optical approach to investigate lower temperature and novel physical phenomena in microgravity based on the ultra-cold quantum degenerate gas of ^{87}Rb , has been deployed. The development of the CAPR is technically challenging, since the rack has to satisfy the restrictions on its size, weight, and the power consumption and it also has to survive the vibration and impact during the launch and work well after the launch. In this article, we report the design, realization, and the validation of the CAPR which consists of a physical system, an all-fiber optical system, and an electrical driving and controlling system. We also demonstrate the feasibility of CAPR by realizing a ^{87}Rb BEC in an optical dipole trap (ODT) and its robustness by repeating the quantum degenerate gases after system integration and space qualification experiments. This paper is organized as following. Section II describes the integrated scheme of the physical system, which includes the vacuum apparatus, the magnetic coils, and the optical modules. The all-fiber optical system is described in Section III, including the 780 nm lasers and the 1064 nm lasers for cooling, trapping, evaporating, and imaging rubidium atoms. The process of BEC production is shown in Section IV. A quantum degenerate gas with 1.2×10^5 atoms and a temperature below 30 nK was realized by forced evaporative cooling in the crossed ODT. The system integration and the space qualification experiments were introduced in Section V. The quantum degenerate gases can be re-achieved after system integration, the thermal and the vibration test. The conclusion is given in Section VI.

II. THE PHYSICAL SYSTEM

The physical system is the subsystem in which the experiments on the atoms are performed, as shown in Fig. 1. It was limited by the payload assigned by the Chinese space station and was designed to be as compact as possible. The physical system consists of the vacuum apparatus, the magnetic coils, and the optical modules. They are all firmly fixed to survive the vibrations and impacts during the launch phase. The optical modules transmit the laser from the fibers to the vacuum chambers and provide the required optical field.

The vacuum apparatus is the main part of the physical system, and it houses all the magnetics coils and the optical modules. The vacuum apparatus mainly includes an atomic source, a two-dimensional magneto-optical trap (2-D MOT) chamber, a science chamber, and several pumps that maintain the ultra-high vacuum. The atomic source can release Rb atoms into the 2-D MOT chamber when heated. An 8 L/s ion pump is connected to the 2-D MOT chamber to maintain the pressure at 5×10^{-7} Pa. A 75 L/s ion pump and two getter pumps are connected to port A7 to maintain the pressure of 2×10^{-9} Pa in the science chamber. A differential pumping stage connects the two vacuum chambers so that the Rb atoms can pass from the 2-D MOT chamber to the science chamber, while the pressure difference can be more than two orders of magnitude at the same time [36].

All magnetic coils are fixed on the vacuum chambers and provide the required magnetic field. Two pairs of square coils provide the quadruple magnetic field for 2-D MOT. Each pair works in an anti-Helmholtz configuration, and the two pairs produce an equal and opposite magnetic field along the direction of the atomic beam in the 2-D MOT chamber. A pair of coils for 3-D MOT generate a quadruple magnetic field that can produce a magnetic gradient from 0 G/cm to 60 G/cm in the y-direction.

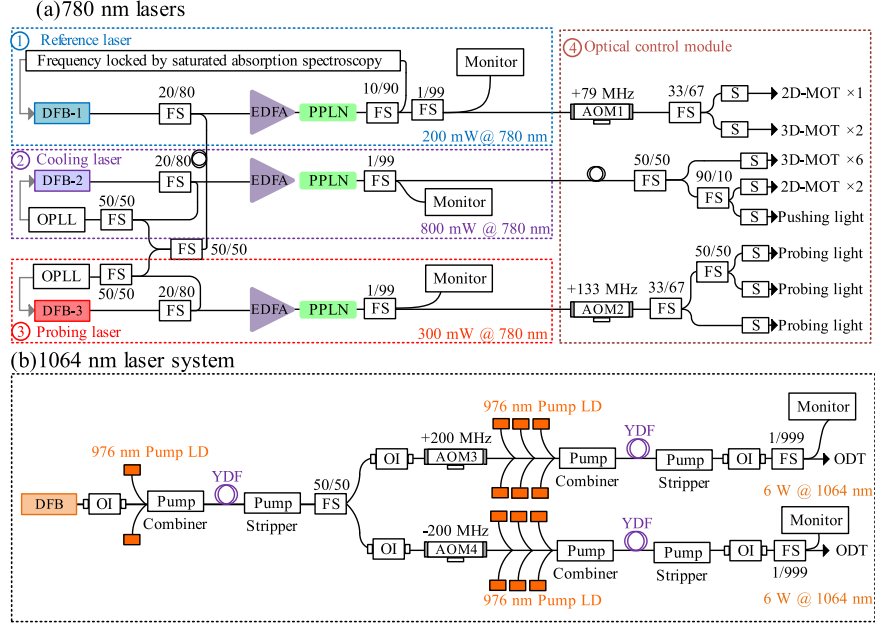


Fig. 2. The functional schematic of the all-fiber optical system including (a) the 780 nm lasers and (b) the 1064 nm lasers. (a): The reference laser, the cooling laser, and the probing laser of the 780 nm laser system are the second harmonic generated by the DFB 1560 nm laser via PPLN. The 780 nm lasers are amplified by EDFA before the PPLN crystals, and the power of the reference, cooling, and probing laser is 200 mW, 800 mW, and 300 mW respectively. The frequency of the reference laser is locked by saturated absorption spectroscopy, and the cooling laser and the probing laser are locked to the reference laser by OPLLs. After the PPLN crystals, each 780 nm laser is sent to the optical control module to split, combine, frequency control and power adjust for cooling, trapping, manipulating, and detecting rubidium atoms. FS: Fiber splitter, S: Shutter, EDFA: Erbium-doped fiber amplifier, PPLN: Periodically poled lithium niobate, AOM: Acousto-optic modulator. (b): The 1064 nm laser system takes a single frequency DFB 1064 nm laser as the source, which is first amplified by a YDFA. The output of the first stage amplification is equally divided into two parts and fed into the respective AOMs and then the second stage amplifiers. This results in a 1064 nm laser system with two output powers of higher than 6W. The laser power of the AOM's output is closed-loop controlled, while the laser power of the final stage amplifier's output is only open-loop controlled. YDFA: Ytterbium-doped fiber amplifier, LD: Laser Diode.

Three pairs of Helmholtz coils are used to balance the ambient magnetic field along each direction in order to decrease the temperature of the molasses.

The optical modules transport the lasers from the all-fiber optical system into the vacuum chambers and provide the required optical field to cool, trap, and image the ^{87}Rb atoms. All components such as collimators, lenses, polarizing beam-splitter cubes, wave plates, mirrors, and cameras, are minimized and fixed in the optical modules to ensure the pointing stability after the vibrations and shocks. The 2-D MOT optical modules shape and guide the 2-D MOT beams, including two 2-D MOT cooling beams, one 2-D MOT repumping beam, and one pushing beam. Two 2-D MOT cooling beams travel along the y - and z -directions into the 2-D MOT chamber and are reflected, and one of them is combined with the 2-D MOT repumping beam. The pushing light travels along the x -direction and pushes the atoms into the science chamber through the port A1. Six 3-D MOT cooling beams pass through ports A2, A5, A8, A11 and the other two ports in the y -direction. Two repumping beams for 3-D MOT are combined with two cooling beams in the fiber and pass through ports A5 and A11. Three perpendicular absorption imaging systems are placed in three orthogonal directions to comprehensively acquire information of the atomic clouds. They include probing lights and cameras in A3-A9, A6-A12, and y -directions. The magnifications along each direction are 0.76, 0.76, and 1.6, respectively. The ODT beams with a waist of $72\ \mu\text{m}$ crossing at an angle of 60° are guided into the science

chamber through ports A4 and A8 and terminated at ports A10 and A2 by the optical absorbers. All the ODT beams of CAPR can be adjusted by the optical wedge pairs. In addition, a close-looped piezoelectric-driven reflector is integrated into the optical module at port A4 and is used to fine tune the direction of the ODT beam with an adjustment accuracy and range of $1\ \mu\text{m}$ and $237\ \mu\text{m}$ in the y -direction respectively, which is important to increase the stability of the optical path direction and compensate the direction changed by the shock and vibration during the launch.

III. THE ALL-FIBER OPTICAL SYSTEM

The realization of BEC all-optically in microgravity requires optical system that (i) provides high reliability, (ii) is easy to integrate and transport, (iii) has high-power narrow-linewidth lasers to collect and evaporate atoms to BEC, and (iv) has capable of performing the complex switching and control procedures of all lasers for experimental sequences. For these reasons, an all-fiber optical system was constructed for CAPR. The optical system consists of two parts, the 780 nm lasers and the 1064 nm lasers, as shown in Fig. 2(a) and (b). The 780 nm lasers are closely resonant with rubidium atoms, so they can cool and trap the ^{87}Rb atoms from a room-temperature background in MOT. The 1064 nm lasers are far-off resonant with rubidium atoms, so they can capture and evaporate ^{87}Rb atoms to quantum degeneracy with nano-kelvin temperatures. The optical system is

connected to the optical modules with polarization-maintaining (PM) fibers.

The 780 nm lasers are shown in Fig. 2(a) and consist of a reference laser ①, a cooling laser ②, a probing laser ③, and an optical control module ④. All 780 nm lasers start from the 1560 nm distributed-feed-back (DFB) laser diodes, since the commercial telecommunication fiber components have been tested for cooling alkali-earth species [37], [38] in microgravity [39], [40]. The 780 nm lasers are obtained after the seeds being amplified by an erbium-doped fiber amplifier (EDFA) and then frequency-doubled by a periodically poled lithium niobate crystal (PPLN). The output powers of the reference, cooling, and probing laser are 200 mW, 800 mW, and 300 mW, respectively. The frequency of the reference laser is locked by saturated absorption spectroscopy [41] on the crossover transition between the ^{87}Rb $|5^2S_{1/2}, F = 1\rangle$ to $^{87}\text{Rb}|5^2P_{3/2}, F' = 1\rangle$ and $^{87}\text{Rb}|5^2P_{3/2}, F' = 2\rangle$, which is red-detuned by 79 MHz from the $^{87}\text{Rb}|5^2S_{1/2}, F = 1\rangle \rightarrow |5^2P_{3/2}, F' = 2\rangle$ transition. The frequencies of the cooling laser and the probing laser are locked to the reference laser via optical phase-locked loops (OPLL) [42] and can both be tuned from 0 to -20Γ ($\Gamma = 6.06$ MHz, the natural linewidth of the ^{87}Rb D₂ line) to the ^{87}Rb D_{2A} $|5^2S_{1/2}, F = 2\rangle \rightarrow |5^2P_{3/2}, F' = 3\rangle$ transition.

An optical control module is used to split the 780 nm laser into fifteen functional laser beams (one 2-D MOT repumping beam, two 3-D MOT repumping beams, two 2-D MOT cooling beams, six 3-D MOT cooling beams, one pushing beam, and three probing beams), as shown in Fig. 2(a) ④. The optical control module can switch, split, frequency control, and power adjust the lasers by acousto-optic modulators (AOM), fiber splitters (FS), shutters (S), and microelectromechanical systems (MEMS)-based variable attenuators. The repumping laser is shifted by the AOM1 (+79 MHz) to be resonant to the ^{87}Rb D_{2B} $|5^2S_{1/2}, F = 1\rangle \rightarrow |5^2P_{3/2}, F' = 2\rangle$ transition. The AOM2 (+133 MHz) modulates the probing laser and generates two pulses during one absorption imaging phase.

The 1064 nm lasers for ODT with two outputs over 6W are shown in Fig. 2(b). Two lasers share the same seed and the same first stage amplifier before being divided into two equal parts by the FS to make the system as compact as possible. The seed is a 1064 nm DFB laser, and the two-stage amplifiers are both Ytterbium-doped fiber amplifiers (YDFA) [43] pumped by 976 nm lasers. Before the second stage amplifiers, two lasers are respectively blue detuned and red detuned 200 MHz by two AOMs (AOM3, AOM4), so the spatial interference formed by the two lasers temporally varies rapidly enough and hardly induces stimulation to the atoms. More than 6W of two outputs are obtained after the second amplification.

The reason for placing the AOMs between the two stage amplifiers is that the maximum transmission rate of the fiber-packed AOM is less than 60%, and the maximum tolerated power of the AOM is only 5W. If the AOMs were placed after the second stage amplifiers, the maximum laser power for an ODT beam would be 3W or less, and the efficient trap depth of the crossed ODT is about 213 μK [44], [45] with a waist of 72 μm , which is insufficient to load adequate atoms in the ODT. The laser power of the AOM's output is closed-loop controlled by the RF

power driving AOM3 and AOM4, while the laser power of the final stage amplifier's output is only open-loop controlled. The reason for this is that during the process of evaporative cooling of the atoms by ramping down the ODT power, the lower the ODT power, the more precise the power control need to be. During the open-loop phase through the final stage amplifiers, the ODT power varies between 6W and 80 mW. During the closed-loop phase through the AOM3 and AOM4, the ODT power ranges from 80 mW to zero.

IV. EXPERIMENT METHODS AND RESULTS

The process of ultracold quantum degenerate gases BEC production is developed and realized based on the specially designed for CAPR, as shown in Fig. 3. The ^{87}Rb atoms are cooled and collected from the background by the 2-D MOT, and then be pushed into the science chamber by the pushing beam and recaptured by the 3-D MOT. The 2-D MOT lights are split into three Gaussian beams with 13 mm diameter and 3 mm spacing. The power of each 2-D MOT cooling beam is 60 mW, and the power of the 2-D MOT repumping beam is 10 mW. The 2-D MOT cooling laser is red-detuned by 18 MHz from ^{87}Rb D_{2A} $|5^2S_{1/2}, F = 2\rangle \rightarrow |5^2P_{3/2}, F' = 3\rangle$ transition, and the repumping laser is resonant with the ^{87}Rb D_{2B} $|5^2S_{1/2}, F = 1\rangle \rightarrow |5^2P_{3/2}, F' = 2\rangle$ transition. There are two pairs of square 2-D MOT coils aligned along the y- and z- directions, producing the gradient of magnetic induction density along each direction of about 10 G/cm. The four magnetic coils are driven separately so that the direction of the atomic beam into the differential tube can be fine-tuned, so that the 3-D MOT loading rate can be optimized. The pushing beam, at the same frequency as the cooling beam, is collimated to a diameter of 2 mm with a power of 12 mW. The 3-D MOT consists of six cooling beams, two repumping beams and a pair of quadruple magnetic coils. The diameters of all 3-D MOT lights are 18 mm. The power of each 3-D MOT cooling beam is about 20 mW, and the power of each 3-D MOT repumping beam is 10 mW. The frequencies of the 3-D MOT cooling and the repumping lights are the same as the 2-D MOT cooling and the repumping lights. The magnetic flux density gradient of the 3-D MOT quadruple coils is 14 G/cm, and the coils are connected in series so that they can be turned on and off simultaneously.

The MOT loading process takes 10s and 2×10^9 ^{87}Rb atoms can be captured with a temperature of 500 μK . After MOT loading, the compressed MOT (CMOT) [46] is implemented to increase the density of atoms by ramping up the magnetic flux density gradient to 48 G/cm and being held for 30 ms. The temporarily dark MOT (TDM) [20] follows the CMOT and increases the density of atoms to over $1 \times 10^{12}\text{cm}^{-3}$. The power of each repumping beam is decreased from 10 mW to 10 μW during the TDM, and the process lasts for 100 ms. Following the TDM, the molasses [47], [48] is applied by turning off the quadruple magnetic field and ramping the detuning of the cooling lights from -18 MHz to -102 MHz within 6 ms and lasting for 20 ms. During the molasses, the power of each 3-D MOT cooling beam is linearly decreased from 20 mW to 1.3 mW within 6 ms and maintained for the remaining 20 ms.

	3D-MOT	CMOT	Dark Spot	Molasses	ODT Hold	Forced Evaporation	TOF	Image
Time (ms)	10000	30	100	26	100	11181	15	200
3D-MOT magnetic field	14 G/cm	48 G/cm	14 G/cm	0 G/cm				
3D-MOT Cooling Power	20 mW			1.3 mW	0 mW			
3D-MOT Cooling Frequency	-18 MHz			-102 MHz				
3D-MOT Repumping Power	10 mW		10 μ W		0 mW			10 mW
Image Probing Power	0 mW							100 μ W
Optical Dipole Trap Power	6 W				0.8 W	0.08 W	0.24 W	0 mW

Fig. 3. The time sequence of realization of BEC on the CAPR. After 10s 3-D MOT loading, the atoms are compressed by the CMOT to increase density. The temporarily dark MOT comes after the CMOT and holds for 100 ms, which can increase the atomic density to more than $1 \times 10^{12} \text{ cm}^{-3}$. Then molasses is then applied and the temperature of the atoms can be lowered to $26 \mu\text{K}$. After 100 ms ODT holding, 3×10^6 atoms can be reserved in the ODT. The BEC can be achieved after forced evaporative cooling by ramping down the power of the ODT. The BECs are imaged after 15 ms of ballistic expansion.

The temperature of the atoms can be lowered to $26 \mu\text{K}$ after the molasses process. The ODT laser is turned on simultaneously with the MOT loading process. The ODT holds for 100 ms more after the molasses to ensure that all atoms out of the trap can fly away, so that the number of atoms in the trap can be accurately measured. All phases, such as MOT, CMOT, TDM and molasses, are optimized for the improvement of the ODT loading. In addition, the 3-D MOT repumping lights are turned off 1 ms before the turning off the cooling lights to ensure the atoms being pumped to the $|5^2 S_{1/2}, F = 1\rangle$ state, and the BEC achieved in the ODT are in the $F = 1$ state with $m_F = (0, \pm 1)$ states [32]. Finally, 3×10^6 ^{87}Rb atoms can be reserved in crossed-beam section of the ODT.

The evaporative cooling starts after 100 ms being held in the ODT. Initially, the power of each 1064 nm laser beam is 6W, which corresponds to the effective trap depth as $355 \mu\text{K}$ and the trap frequency as $(\omega_x, \omega_y, \omega_z) = 2\pi \times (1.8, 2.3, 1.4)\text{kHz}$. The atoms are evaporated by ramping down the power of the ODT laser, and the ramp is divided into several linear segments. The duration and slope of each segment are optimized by maximizing the optical depth (OD) to maintain “runaway evaporative cooling” [49]. The path of optimized evaporation on the CAPR is shown in Fig. 4. In the first phase, the power of the ODT laser is linearly decreased from 6W to 800 mW within 3s and the temperature of the atoms is lower to $10 \mu\text{K}$. Then, the power ramps to 150 mW within 2s, the temperature reaches $2.3 \mu\text{K}$ and the atom numbers in the ODT is about 7×10^5 . In the next phase, the power is ramped down to 80 mW within 1s, 4.7×10^5 atoms are reserved in the ODT with the temperature of about $1 \mu\text{K}$. Our evaporation is efficient because as the depth of the ODT decreases, the temperature of the atomic cloud decreases, the density increases, and the phase space density increases. The ODT power is then decreased to 48 mW within 2s, about 3×10^5 atoms can be reserved in the ODT with the temperature of about 411 nK. When the power is ramped down to 40 mW, the atomic cloud starts to transfer to BEC with a temperature of 240 nK , which is below the phase transition temperature $T_c \approx 400 \text{ nK}$. The phase space density $\text{PSD} = n\lambda_{\text{th}}^3$ is greater than 2.612 after the phase transition, and $\lambda_{\text{th}} = \sqrt{2\pi\hbar/(mk_B T)}$ is the de Broglie wavelength of the atoms and n is the density of

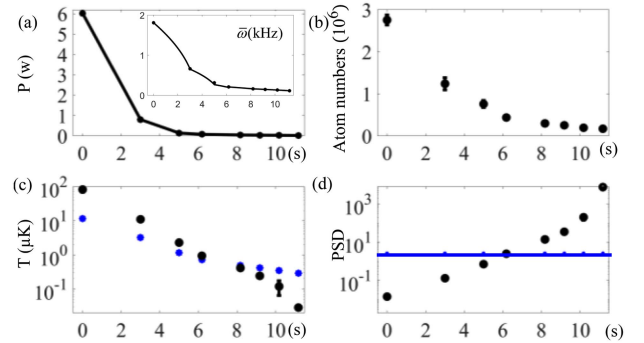


Fig. 4. Path of evaporation on CAPR. (a): The power (solid black line) of the 1064 nm laser versus time during evaporative cooling and the corresponding theoretical trap frequency $\bar{\omega}$ (solid black line) are insert. (b): Atom numbers reserved in the ODT versus time. (c): Atomic temperature (black circle) and the critical temperature T_c (blue circle) versus time. (d): PSD (black circle) versus time. The $\text{PSD} = 2.612$ at the phase transition is shown as a blue line.

the atomic cloud in the ODT [50]. When the power of the laser is reduced below 40 mW, a clear bimodal distribution appears. The spatial distribution of atomic cloud before and after the phase transition is shown in Fig. 5. As shown in Fig. 5(a), the power of the ODT laser is above 40 mW, the free expansion after the time-of-flight (TOF) is isotropic, and the atomic cloud is classical. The condensate, which is not isotropic after 15 ms of free expansion, starts to emerge with lower ODT power. While the power of the ODT laser decreases to 38 mW, the condensate fraction is 36% as shown in Fig. 5(b). When the power of ODT becomes lower, the condensate fraction continues to increase. The condensate fraction is higher than 70%, as shown in Fig. 5(c), while the ODT power is 36 mW. In Fig. 5(d) and (e), the classical components of the atomic cloud cannot be observed, while the ODT laser power is less than 30 mW. They can be considered as experimentally “pure” condensate.

The process for BEC is completed after an evaporation time of 11.2s with a power of 24 mW, the trap frequency and trap depth is $(\omega_x, \omega_y, \omega_z) = 2\pi \times (115, 147, 89)\text{Hz}$ and $k_B \times 1.4 \mu\text{K}$. The temperature of the atoms is below 30 nK which $T = (T_x + T_y)/2$,

$$T_{x(y)} = \frac{m}{2k_B} \left(\frac{\omega_{x(y)}^2}{1 + \omega_{x(y)}^2 t^2} r_{x(y)} t^2 \right), \quad (1)$$

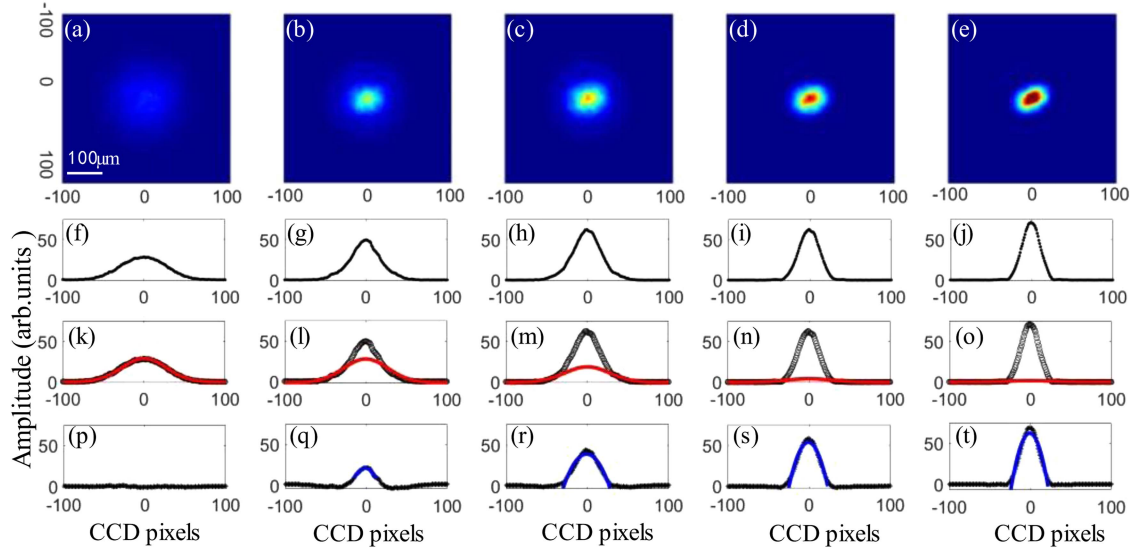


Fig. 5. The phase transition to BEC. (a)~(e): Pseudo color image of the atomic cloud after 15 ms of free expansion, showing the process of phase transition. (a): An isotropic distribution of classic atomic cloud just before the BEC transition. (b): A bimodal distribution after the BEC transition with a condensate fraction of 36%. (c): A bimodal distribution after the BEC transition with a condensate fraction greater than 70%. (d): “Pure” condensate with peak optical depth of 2.8. (e): “Pure” condensate with peak optical depth of 3.6. (f)~(j): Areal density distribution of atoms corresponding to figures(a~e) along the x-direction. (k~o): The gaussian fits of the thermal component of figure(a~e), as shown in red. (p~t): The parabolic fits of the condensed fraction of figure(a~e), as shown in blue. The size of a single pixel is $2.16 \mu\text{m}$.

$\omega_{x(y)}$ is the trap frequency along the x (y) direction, $r_{x(y)}$ is the Gaussian radius of the atoms after 15 ms of free expansion.

V. SYSTEM ASSEMBLY, INTEGRATION, AND ENVIRONMENT TEST

System assembly, integration, and environmental test is another essential procedure for the validation of the CAPR. The optimal assembly and integration scheme makes sure the system satisfies the space station’s restrictions on payload size and weight. It also ensures that the rack can survive the vibrations and impacts during the launch. All the heating elements cling well to the water-cooled heat sink after the assembly. Thermal test and mechanical test are the two main environmental tests. Thermal cycling test is applied to verify the temperature adaptability of the rack, while the mechanical test simulates the rack during the launch. After the assembly, all the sub-systems are integrated into a standard rack for the CSS.

The science chamber, as shown in Fig. 1, is surrounded by a 3-layer magnetic shields. The vacuum apparatus with the magnetic shield is mounted in a topless aluminum box that serves as the main fixed structure of the physical system. The heat accumulated in the magnetic shield is transferred to the water-cool heat sink installed on the side of the aluminum box via two Aluminum/Ammonia heat pipes outside the quadrupole coils. All the optical fibers and the wires connected to the science chamber pass through the magnetic shield at the same location as the heat pipes. The assembled physical system is approximately $590 \text{ mm} \times 930 \text{ mm} \times 510 \text{ mm}$ in dimensions with a mass of 170 kg.

The 780 nm laser system integrates all the optical and the electrical components into one aluminum box, and connect to the physical system with three optical fibers. The 1064 nm laser

system integrates all the optical and the electrical components into another aluminum box, and connect to the physical system with eight optical fibers. Each laser box is mounted on a water-cooled hear sink, and the optical and electrical components are separately integrated in distinct layers. The electrical driving and controlling system receive the signals from the instruction system, transmits them to the physical system, the 780 nm and 1064 nm laser system, and stores all the experiment results and the engineering parameters. Laser systems and the electrical driving and controlling system are of the similar size and weight, which are $550 \text{ mm} \times 470 \text{ mm} \times 280 \text{ mm}$ and less than 50 kg.

After assembly, the peak power consumption of the CAPR performing BEC experiment sequence is 600W and all the heat dissipation depends on the water-cooled loops. The thermal cycling test verified whether the whole rack would work well after being exposed in the environment with great temperature change. The fiber laser systems experienced 12.5 thermal cycles with a temperature range of $5 \text{ }^\circ\text{C}$ to $35 \text{ }^\circ\text{C}$, while the lowest temperature and highest temperature holds for three hours. The physical system also experienced 12.5 thermal cycles with a temperature range of $10 \text{ }^\circ\text{C}$ to $30 \text{ }^\circ\text{C}$, while the lowest temperature and highest temperature holds for four hours. The electrical driving and controlling system experienced 3.5 thermal cycles with a temperature range of $-10 \text{ }^\circ\text{C}$ to $60 \text{ }^\circ\text{C}$, while the lowest temperature and highest temperature holds for three hours. The temperature changed at a rate of $5 \text{ }^\circ\text{C/h}$.

Sinusoidal vibration is mostly used to test a device’s resonance frequency. The standard diagnostic procedure starts and ends with a resonance scan for each axis. Afterwards, a random vibration test lasts for 60s with the acceleration of $4.2 g_{\text{RMS}}$. Before and after the mechanical test, the optimal experiment sequence for BEC had been continuously executed for twenty-seven times

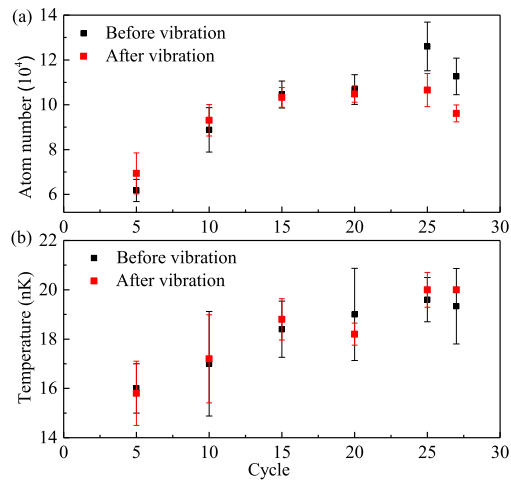


Fig. 6. The parameter of BEC before and after the mechanical test. (a): Atom number of the BEC over nearly 30 cycles. (b): Temperature of the BEC over nearly 30 cycles.

in thirty minutes, and the results were shown in Fig. 6. We averaged every five adjacent results, including the atom numbers and the atomic temperatures, and compared them in the figure. The environment temperature was both set to 23 °C during the experiments. As shown in the figure, the atom number and the atomic temperatures before and after the mechanical test are well consistent with each other, and their trends along time are nearly the same. Through these results, we can draw a conclusion that, after the mechanical test, the rack nearly performed as well as itself before the test.

VI. CONCLUSION

In summary, the CAPR is developed and we report the design, realization, and the validation of the rack. We describe the integrated physical system and the all-fiber optical system, and demonstrate the feasibility of CAPR by experimentally generating an ⁸⁷Rb BEC in a ground-based laboratory, which maintains the ability of achieving BEC after integration and environment test. The integrated physical system provides the necessary vacuum, magnetic field, and optical field for performing experiments with ultra-cold atoms. The optical system provides lasers for preparing a BEC of ⁸⁷Rb, and the all-fiber scheme makes the system reliable and compact. A quantum degenerate gas was produced by forced evaporative cooling in the crossed ODT with 1.2×10^5 atoms and a temperature below 30 nK. The integrated CAPR satisfies the restrictions on the size, weight, and power consumption, and performs well after the space environmental qualification tests. The CAPR offers the ability to lower the temperature of the atoms to pico- or even femto-kelvin by deep cooling. It also provides the possibility of observing and understanding novel physical phenomena in microgravity and the potential for high-precision quantum measurement applications.

ACKNOWLEDGMENT

The authors would like to thank Shuyu Zhou for helpful guidance. The authors would also like to thank the contribution

from Lijia Wang, Kedi Xie, Shuang Tang, Guibing Wang, Liping Chen, Zhichao Xing, Minghui Wen, Fenhong Song, Jianxin Huang, Aoqi Zhu, Aijun Zeng, Rui Li, Taijun Pan, Xin Zhou, Yi Hong, Hongxin Liu, Hongwei Luo, Yiyan Yu, Shengnan Hu, Xingchen Wan, Wei Shi, and Pengfei Li.

REFERENCES

- [1] W. Meissner and R. Ochsenfeld, "Ein neuer effekt bei eintritt der supraleitfähigkeit," *Naturwissenschaften*, vol. 21, no. 44, pp. 787–788, 1933.
- [2] P. Kapitza, "Viscosity of liquid helium below the λ -point," *Nature*, vol. 141, no. 3558, pp. 74–74, 1938.
- [3] J. F. Allen and A. Misener, "Flow phenomena in liquid helium II," *Nature*, vol. 142, no. 3597, pp. 643–644, 1938.
- [4] M. H. Anderson, J. R. Ensher, M. R. Matthews, C. E. Wieman, and E. A. Cornell, "Observation of Bose-Einstein condensation in a dilute atomic vapor," *Science*, vol. 269, no. 5221, pp. 198–201, Jul. 1995, doi: [10.1126/science.269.5221.198](https://doi.org/10.1126/science.269.5221.198).
- [5] B. DeMarco and D. S. Jin, "Onset of Fermi degeneracy in a trapped atomic gas," *Science*, vol. 285, no. 5434, pp. 1703–1706, Sep. 1999, doi: [10.1126/science.285.5434.1703](https://doi.org/10.1126/science.285.5434.1703).
- [6] M. A. Kasevich, E. Riis, S. Chu, and R. G. DeVoe, "RF spectroscopy in an atomic fountain," *Phys. Rev. Lett.*, vol. 63, no. 6, pp. 612–615, Aug. 1989, doi: [10.1103/PhysRevLett.63.612](https://doi.org/10.1103/PhysRevLett.63.612).
- [7] M. Kasevich and S. Chu, "Atomic interferometry using stimulated Raman transitions," *Phys. Rev. Lett.*, vol. 67, no. 2, pp. 181–184, Jul. 1991, doi: [10.1103/PhysRevLett.67.181](https://doi.org/10.1103/PhysRevLett.67.181).
- [8] M. Kasevich and S. Chu, "Measurement of the gravitational acceleration of an atom with a light-pulse atom interferometer," *Appl. Phys. B*, vol. 54, no. 5, pp. 321–332, 1992.
- [9] S. Chu, L. Hollberg, J. E. Bjorkholm, A. Cable, and A. Ashkin, "Three-dimensional viscous confinement and cooling of atoms by resonance radiation pressure," *Phys. Rev. Lett.*, vol. 55, no. 1, 1985, Art. no. 48.
- [10] A. Aspect, J. Dalibard, A. Heidmann, C. Salomon, and C. Cohen-Tannoudji, "Cooling atoms with stimulated emission," *Phys. Rev. Lett.*, vol. 57, no. 14, pp. 1688–1691, Oct. 1986, doi: [10.1103/PhysRevLett.57.1688](https://doi.org/10.1103/PhysRevLett.57.1688).
- [11] A. Aspect, E. Arimondo, R. Kaiser, N. Vansteenkiste, and C. Cohentannoudji, "Laser cooling below the one-photon recoil energy by velocity-selective coherent population trapping," *Phys. Rev. Lett.*, vol. 61, no. 7, pp. 826–829, Aug. 1988, doi: [10.1103/PhysRevLett.61.826](https://doi.org/10.1103/PhysRevLett.61.826).
- [12] M. Kasevich and S. Chu, "Laser cooling below a photon recoil with three-level atoms," *Phys. Rev. Lett.*, vol. 69, no. 12, pp. 1741–1744, Sep. 1992, doi: [10.1103/PhysRevLett.69.1741](https://doi.org/10.1103/PhysRevLett.69.1741).
- [13] A. E. Leanhardt et al., "Cooling Bose-Einstein condensates below 500 picokelvin," *Science*, vol. 301, no. 5639, pp. 1513–1515, Sep. 2003, doi: [10.1126/science.1088827](https://doi.org/10.1126/science.1088827).
- [14] P. Medley, D. M. Weld, H. Miyake, D. E. Pritchard, and W. Ketterle, "Spin gradient demagnetization cooling of ultracold atoms," *Phys. Rev. Lett.*, vol. 106, no. 19, May 2011, Art. no. 195301, doi: [10.1103/PhysRevLett.106.195301](https://doi.org/10.1103/PhysRevLett.106.195301).
- [15] C. Deppner et al., "Collective-mode enhanced matter-wave optics," *Phys. Rev. Lett.*, vol. 127, no. 10, Sep. 2021, Art. no. 100401, doi: [10.1103/PhysRevLett.127.100401](https://doi.org/10.1103/PhysRevLett.127.100401).
- [16] D. C. Aveline et al., "Observation of Bose-Einstein condensates in an earth-orbiting research lab," *Nature*, vol. 582, no. 7811, pp. 193–197, Jun. 2020, doi: [10.1038/s41586-020-2346-1](https://doi.org/10.1038/s41586-020-2346-1).
- [17] N. Gaaloul et al., "A space-based quantum gas laboratory at picokelvin energy scales," *Nature Commun.*, vol. 13, 2022, Art. no. 7889.
- [18] T. van Zoest et al., "Bose-Einstein condensation in microgravity," *Science*, vol. 328, no. 5985, pp. 1540–1543, Jun. 2010, doi: [10.1126/science.1189164](https://doi.org/10.1126/science.1189164).
- [19] H. Muntinga et al., "Interferometry with Bose-Einstein condensates in microgravity," *Phys. Rev. Lett.*, vol. 110, no. 9, Mar. 2013, Art. no. 093602, doi: [10.1103/PhysRevLett.110.093602](https://doi.org/10.1103/PhysRevLett.110.093602).
- [20] C. Vogt et al., "Evaporative cooling from an optical dipole trap in microgravity," *Phys. Rev. A*, vol. 101, no. 1, 2020, Art. no. 013634.
- [21] C. Lotz, Y. Wessarges, J. Hermsdorf, W. Ertmer, and L. Overmeyer, "Novel active driven drop tower facility for microgravity experiments investigating production technologies on the example of substrate-free additive manufacturing," *Adv. Space Res.*, vol. 61, no. 8, pp. 1967–1974, 2018.

- [22] G. Condon et al., "All-optical Bose-Einstein condensates in microgravity," *Phys. Rev. Lett.*, vol. 123, no. 24, Dec. 2019, Art. no. 240402, doi: [10.1103/PhysRevLett.123.240402](https://doi.org/10.1103/PhysRevLett.123.240402).
- [23] G. Stern et al., "Light-pulse atom interferometry in microgravity," *Eur. Phys. J. D*, vol. 53, no. 3, pp. 353–357, 2009.
- [24] M. Langlois, L. De Sarlo, D. Holleville, N. Dimarcq, J.-F. Schaff, and S. Bernon, "Compact cold-atom clock for onboard timebase: Tests in reduced gravity," *Phys. Rev. Appl.*, vol. 10, no. 6, 2018, Art. no. 064007.
- [25] R. Geiger et al., "Detecting inertial effects with airborne matter-wave interferometry," *Nature Commun.*, vol. 2, Sep. 2011, Art. no. 474, doi: [10.1038/ncomms1479](https://doi.org/10.1038/ncomms1479).
- [26] B. Barrett et al., "Dual matter-wave inertial sensors in weightlessness," *Nature Commun.*, vol. 7, no. 1, pp. 1–9, 2016.
- [27] D. Becker et al., "Space-borne Bose-Einstein condensation for precision interferometry," *Nature*, vol. 562, no. 7727, pp. 391–395, Oct. 2018, doi: [10.1038/s41586-018-0605-1](https://doi.org/10.1038/s41586-018-0605-1).
- [28] M. D. Lachmann et al., "Ultracold atom interferometry in space," *Nature Commun.*, vol. 12, no. 1, Feb. 2021, Art. no. 1317, doi: [10.1038/s41467-021-21628-z](https://doi.org/10.1038/s41467-021-21628-z).
- [29] L. Liu et al., "In-orbit operation of an atomic clock based on laser-cooled ^{87}Rb atoms," *Nature Commun.*, vol. 9, no. 1, 2018, Art. no. 2760.
- [30] E. R. Elliott, M. C. Krutzik, J. R. Williams, R. J. Thompson, and D. C. Aveline, "NASA's cold atom lab (CAL): System development and ground test status," *Npj Microgr.*, vol. 4, no. 1, pp. 1–7, 2018.
- [31] K. Frye et al., "The Bose-Einstein condensate and cold atom laboratory," *Eur. Phys. J. Quantum Technol.*, vol. 8, no. 1, 2021, Art. no. 1.
- [32] M. Barrett, J. Sauer, and M. Chapman, "All-optical formation of an atomic Bose-Einstein condensate," *Phys. Rev. Lett.*, vol. 87, no. 1, 2001, Art. no. 010404, doi: [10.1103/PhysRevLett.87.010404](https://doi.org/10.1103/PhysRevLett.87.010404).
- [33] T. Kinoshita, T. Wenger, and D. S. Weiss, "All-optical Bose-Einstein condensation using a compressible crossed dipole trap," *Phys. Rev. A*, vol. 71, no. 1, 2005, Art. no. 011602.
- [34] R. A. Carollo et al., "Observation of ultracold atomic bubbles in orbital microgravity," *Nature*, vol. 606, no. 7913, pp. 281–286, 2022.
- [35] N. Lundblad et al., "Shell potentials for microgravity Bose-Einstein condensates," *Npj Microgr.*, vol. 5, no. 1, 2019, Art. no. 30.
- [36] Q. Liu et al., "Development of an ultra-high vacuum system for a cold atom physics rack in space," *Vacuum*, vol. 190, 2021, Art. no. 110192.
- [37] R. Thompson, M. Tu, D. Aveline, N. Lundblad, and L. Maleki, "High power single frequency 780 nm laser source generated from frequency doubling of a seeded fiber amplifier in a cascade of PPLN crystals," *Opt. Exp.*, vol. 11, no. 14, pp. 1709–1713, 2003.
- [38] C. Cherfan et al., "Multi-frequency telecom fibered laser system for potassium laser cooling," *Appl. Phys. Lett.*, vol. 119, no. 20, 2021, Art. no. 204001.
- [39] T. Lévêque, L. Antoni-Micollier, B. Faure, and J. Berthon, "A laser setup for rubidium cooling dedicated to space applications," *Appl. Phys. B*, vol. 116, no. 4, pp. 997–1004, 2014.
- [40] D. Sabulsky et al., "A fibered laser system for the MIGA large scale atom interferometer," *Sci. Rep.*, vol. 10, no. 1, pp. 1–14, 2020.
- [41] K. MacAdam, A. Steinbach, and C. Wieman, "A narrow-band tunable diode laser system with grating feedback, and a saturated absorption spectrometer for Cs and Rb," *Amer. J. Phys.*, vol. 60, no. 12, pp. 1098–1111, 1992.
- [42] W. R. Leeb, H. K. Philipp, A. L. Scholtz, and E. Bonek, "Frequency synchronization and phase locking of CO₂ lasers," *Appl. Phys. Lett.*, vol. 41, no. 7, pp. 592–594, 1982.
- [43] S. Sanders et al., "Fiber-coupled M-MOPA laser diode pumping a high-power erbium-doped fiber amplifier," in *Proc. Opt. Fiber Commun.*, 1996, pp. 31–32.
- [44] R. Grimm, M. Weidemüller, and Y. B. Ovchinnikov, "Optical dipole traps for neutral atoms," in *Advances in Atomic, Molecular, and Optical Physics*, Amsterdam, The Netherlands: Elsevier, vol. 42, 2000, pp. 95–170.
- [45] T. Luan et al., "Two-stage crossed beam cooling with ^6Li and ^{133}Cs atoms in microgravity," *Opt. Exp.*, vol. 23, no. 9, pp. 11378–11387, 2015.
- [46] W. Petrich, M. H. Anderson, J. R. Ensher, and E. A. Cornell, "Behavior of atoms in a compressed magneto-optical trap," *J. Opt. Soc. Amer. B*, vol. 11, no. 8, pp. 1332–1335, 1994.
- [47] P. J. Ungar, D. S. Weiss, E. Riis, and S. Chu, "Optical molasses and multi-level atoms: Theory," *J. Opt. Soc. Amer. B*, vol. 6, no. 11, pp. 2058–2071, 1989.
- [48] D. S. Weiss, E. Riis, Y. Shevy, P. J. Ungar, and S. Chu, "Optical molasses and multilevel atoms: Experiment," *J. Opt. Soc. Amer. B*, vol. 6, no. 11, pp. 2072–2083, 1989.
- [49] K. B. Davis, M.-O. Mewes, and W. Ketterle, "An analytical model for evaporative cooling of atoms," *Appl. Phys. B*, vol. 60, no. 2, pp. 155–159, 1995.
- [50] W. Ketterle, D. S. Durfee, and D. Stamper-Kurn, "Making, probing and understanding Bose-Einstein condensates," in *Bose-Einstein Condensation in Atomic Gases*, Amsterdam, The Netherlands: IOS Press, 1999, pp. 67–176.